IT'S YOUR TIME
BE PRECISE

STANDARD IMAGING

Every day we spend **our time** optimizing ways to make QA easy and reliable.

Ask us how our solutions can benefit you.

WWW.STANDARDIMAGING.COM

RESEARCH ARTICLE

Heat management of a compact x-ray source for microbeam radiotherapy and FLASH treatments

Johanna Winter[1,2,3,*] ◉ | Anton Dimroth[4,5,*] ◉ | Sebastian Roetzer[6] |
Yunzhe Zhang[6] | Karl-Ludwig Krämer[6] | Christian Petrich[1,2,3] ◉ |
Christoph Matejcek[1,8] | Kurt Aulenbacher[7,8,9] | Markus Zimmermann[6] |
Stephanie E. Combs[1,2] ◉ | Marek Galek[10] ◉ | Ghaleb Natour[4,5] ◉ |
Michael Butzek[4] ◉ | Jan J. Wilkens[1,3] ◉ | Stefan Bartzsch[1,2] ◉

[1]Department of Radiation Oncology, School of Medicine and Klinikum Rechts der Isar, Technical University of Munich (TUM), Munich, Germany

[2]Institute of Radiation Medicine (IRM), Helmholtz Zentrum München GmbH, German Research Center for Environmental Health (HMGU), Neuherberg, Germany

[3]Physics Department, Technical University of Munich (TUM), Garching, Germany

[4]Central Institute for Engineering, Electronics and Analytics (ZEA-1), Forschungszentrum Jülich GmbH, Jülich, Germany

[5]Faculty of Mechanical Engineering, RWTH Aachen University, Aachen, Germany

[6]Laboratory for Product Development and Lightweight Design, Technical University of Munich (TUM), Garching, Germany

[7]Accelerator Design and Integrated Detectors, Helmholtz Institute Mainz, Mainz, Germany

[8]Institute for Nuclear Physics, Johannes Gutenberg University, Mainz, Germany

[9]GSI Helmholtzzentrum für Schwerionenforschung GmbH, Darmstadt, Germany

[10]Department of Electrical Engineering and Information Technology, University of Applied Sciences Munich, Munich, Germany

Correspondence
Johanna Winter, Institute of Radiation Medicine, Helmholtz Zentrum München GmbH, German Research Center for Environmental Health, Ingolstädter Landstr. 1, 85764 Neuherberg, Germany.
Email: johanna.winter@helmholtz-muenchen.de
Anton Dimroth, Forschungszentrum Jülich, Central Institute for Engineering, Electronics and Analytics (ZEA), Wilhelm-Johnen-Straße 1, Jülich, Nordrhein-Westfalen 52428, Germany
Email: a.dimroth@fz-juelich.de

*Authors Johanna Winter and Anton Dimroth contributed equally.

Abstract

Background: Microbeam and x-ray FLASH radiation therapy are innovative concepts that promise reduced normal tissue toxicity in radiation oncology without compromising tumor control. However, currently only large third-generation synchrotrons deliver acceptable x-ray beam qualities and there is a need for compact, hospital-based radiation sources to facilitate clinical translation of these novel treatment strategies.

Purpose: We are currently setting up the first prototype of a line-focus x-ray tube (LFxT), a promising technology that may deliver ultra-high dose rates (UHDRs) of more than 100 Gy/s from a table-top source. The operation of the source in the heat capacity limit allows very high dose rates with micrometer-sized focal spot widths. Here, we investigate concepts of effective heat management for the LFxT, a prerequisite for the performance of the source.

Methods: For different focal spot widths, we investigated the temperature increase numerically with Monte Carlo simulations and finite element analysis (FEA). We benchmarked the temperature and thermal stresses at the focal spot against a commercial x-ray tube with similar power characteristics. We assessed thermal loads at the vacuum chamber housing caused by scattering electrons in Monte Carlo simulations and FEA. Further, we discuss active cooling strategies and present a design of the rotating target.

Results: Conventional focal spot widths led to a temperature increase dominated by heat conduction, while very narrow focal spots led to a temperature increase dominated by the heat capacity of the target material. Due to operation in the heat capacity limit, the temperature increase at the focal spot was lower than for the investigated commercial x-ray tube. Hence, the thermal stress at the focal spot of the LFxT was considered uncritical. The target shaft and the vacuum chamber housing require active cooling to withstand the high heat loads.

Conclusions: The heat capacity limit allows very high power densities at the focal spot of the LFxT and thus facilitates very high dose rates. Numerical simulations demonstrated that the heat load imparted by scattering electrons requires active cooling.

1 | INTRODUCTION

Every second cancer patient receives radiotherapy treatment,[1] but radiation-induced side effects often limit the treatment efficacy. Two recent radiotherapy approaches have preclinically shown less severe side effects at the same tumor control rates compared to conventional treatments: x-ray microbeam radiation therapy (MRT)[2–4] and ultra-high dose rate (UHDR) radiation therapy (FLASH).[5–7] MRT utilizes spatial fractionation of the dose with a linear array of high-dose, 25- to 100-μm-wide peaks and low-dose, 100- to 400-μm-wide valleys. Treatment efficacy of MRT relies on a high peak-to-valley dose ratio and a sharp dose profile, that is, a steep lateral dose falloff from a peak to its neighboring valleys. High peak dose rates are necessary to diminish the smearing of the micrometer-scaled dose distribution due to organ motion.[8] FLASH radiotherapy utilizes UHDRs, nominally greater than 40 Gy/s, to achieve subsecond treatment fractions.[5,6] Preclinical research has demonstrated that the FLASH effect can lead to a reduction in normal tissue side effects, without compromising the treatment efficacy.[5,9] First clinical studies have already started with electron FLASH treatments at modified linear accelerators.[10] However, clinical linear accelerator generated electron beams with energies up to 10 MeV limit treatments to superficial tumors. Alternative radiation modalities, such as protons or photons, are required for the treatment of deep-seated tumors.

Currently, only large third-generation synchrotrons provide suitable x-ray beam properties that meet the requirements for MRT and x-ray FLASH, namely, very high photon fluxes for UHDRs,[8] x-ray energies in the kilovolt range to facilitate a high peak-to-valley dose ratio, and a small source size for a sharp microbeam dose profile.[4] Due to their enormous size and limited availability, synchrotrons are unlikely to be used for clinical routine. Widespread clinical application of MRT and FLASH urgently require suitable compact and affordable x-ray sources.

One promising source for MRT and FLASH is the line-focus x-ray tube (LFxT) that is based on conventional x-ray tube technology with a strongly eccentric focal spot and a very fast rotating target.[11,12] The LFxT can operate at an electron beam power in the megawatt range, enabling dose rates of 100–200 Gy/s. The strongly eccentric focal spot with a width of only 50 μm features an area of 1 mm^2, and the heat load of the electron beam is distributed over a large focal track area. The micrometer-wide focal spot on the very fast rotating target shifts the thermal properties from heat conduction-dominated to heat capacity-dominated, which strongly reduces the focal spot temperature.[11] The LFxT places extraordinary demands on the electron accelerator and the high-voltage power supply.[12] A major challenge of the LFxT is the heat management when operating at extremely high electron beam currents.

In this paper, we present the main challenges and possible solutions related to the heat management when building an LFxT prototype. Locally at the focal spot, we numerically calculated the temperature increase in both the heat conduction limit and the heat capacity limit and investigated the transition between these limits. The high local temperatures entail thermal stress in the vicinity of the focal spot, which we compared toward the rotating envelope Straton x-ray tube (Siemens Healthineers AG, Erlangen, Germany). With Monte Carlo simulations and finite element analysis (FEA), we investigated the temperature increase of the vacuum chamber due to backscattering electrons. Further, we developed a target design that can withstand the thermal and mechanical stresses of the rotating target using FEA and derived a basic global cooling concept.

2 | MATERIALS AND METHODS

Here, we discuss the requirements of a 90 kW LFxT prototype that we are currently setting up at the Technical University of Munich. Components that are important within the scope of this work are depicted in Figure 1. A thermionic cathode and anode produce a 300 keV electron beam, which propagates along the beamline. Focusing magnets around the beamline shape the
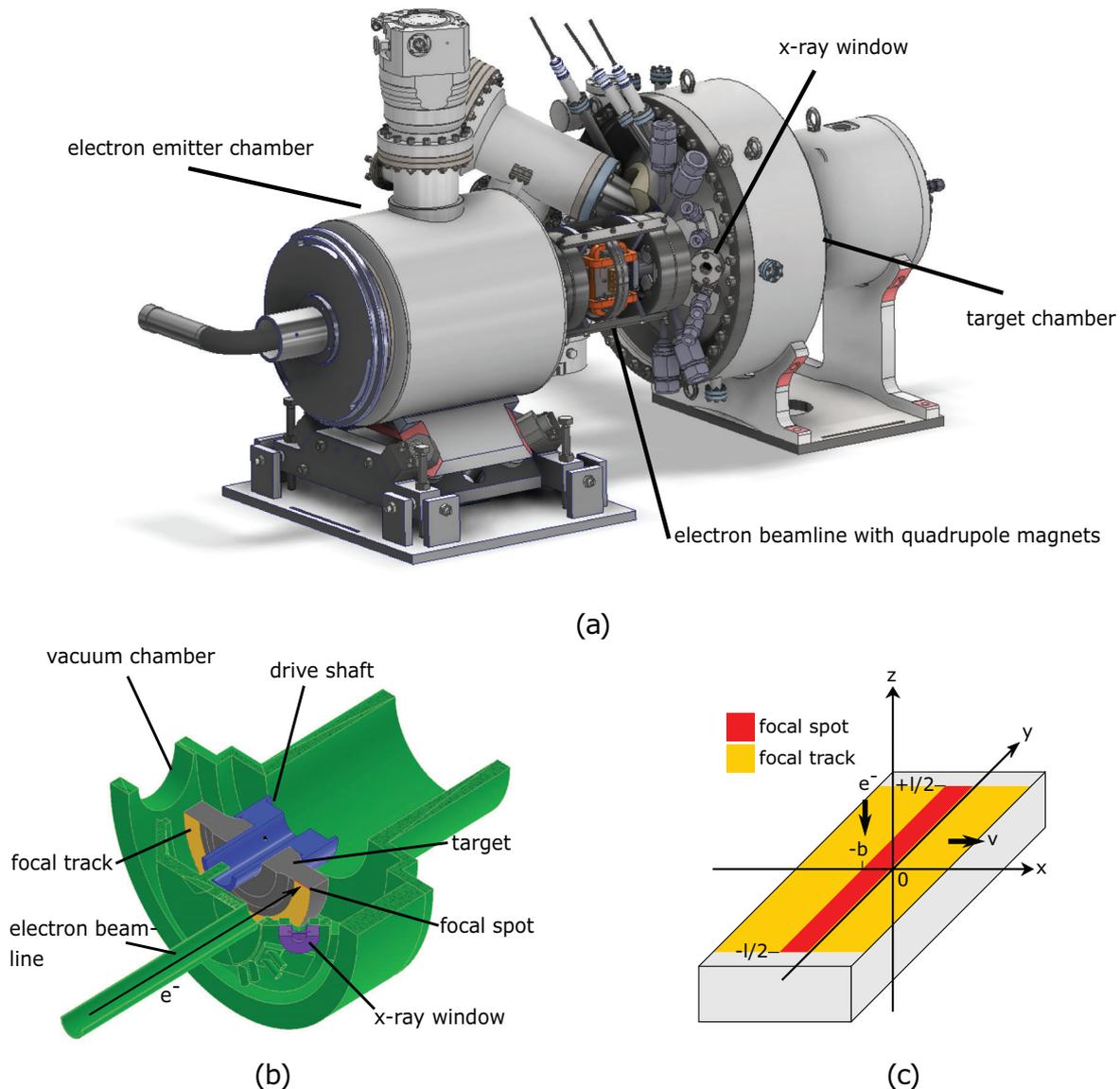
FIGURE 1 (a) CAD model of the LFxT prototype. (b) Half-section of the simplified CAD model used for the simulations. Green represents the vacuum chamber housing (stainless steel AISI 316L), blue the drive shaft (stainless steel AISI 420), gray the target carrier (titanium–zirconium–molybdenum alloy, TZM), yellow the focal track (tungsten–rhenium alloy, W-5%Re), red the focal spot, and purple the x-ray window. (c) Orientation of the focal spot of length $l = 30$ mm and width $b = 50\,\mu$m passing over the target surface with velocity v in positive x-direction (not to scale). The electron beam is oriented in negative z-direction, and the target covers the half space $z < 0$

electron beam into a strongly eccentric focal spot (details in Winter et al.[12]). The electron beam hits the rotating target at the focal spot (red), where a large fraction of the electrons is absorbed, generating heat. Only a small part of the electron energy is converted into the desired x-radiation. Another large fraction of the electrons scatters back and is absorbed by the vacuum chamber. In particular, the x-ray exit window (purple) and heat-sensitive accelerator components are exposed to substantial thermal loads.

The preclinical LFxT prototype will be able to produce dose rates of around 10 Gy/s in 20 cm distance from the focal spot according to Monte Carlo simulations. With an acceleration voltage of 300 kV, the peak-to-valley dose ratio can be above 20 up to a water depth of 100 mm, as demonstrated in Winter et al.[12]

2.1 | Focal spot: Heat conduction limit and heat capacity limit

Due to the inefficient conversion of electron beam power into x-ray beam energy, the target around the focal spot is subject to enormous thermal loads. Effective heat management therefore decides on the performance of an x-ray tube. In rotating target x-ray tubes, the focal spot dimensions, the surface velocity, and the material properties determine the focal spot temperature. While

heat conduction dominates the temperature rise in the focal spot of conventional x-ray tubes (heat conduction limit),[13] its role is negligible for the LFxT, where the focal spot temperature rise is dominated by the heat capacity of the target material (heat capacity limit).[11]

2.1.1 | Derivation of the heat conduction and capacity limit

Heat conduction limit

The temperature increase T_{cond} in the heat conduction limit can be deduced from the heat equation

$$\frac{\partial T_{cond}}{\partial t} - \alpha \Delta T_{cond} = f(\vec{x}, t), \qquad (1)$$

where $\frac{\partial}{\partial t}$ denotes the partial derivative with respect to time; $\alpha = \frac{\lambda}{\rho c}$ the thermal diffusivity with λ the thermal conductivity, ρ the mass density, and c the specific heat capacity; Δ the Laplacian operator; and $f(\vec{x}, t)$ an external heat source in dependence of position $\vec{x} = (x, y, z)$ and time t. For most conventional rotating target x-ray tubes, the electron beam can be considered as a surface heat source of power P_{el}, width b, and length l passing over the surface of a half space ($z < 0$) with velocity v, see Figure 1c. The solution of the three-dimensional heat equation can be obtained by

$$T_{cond} = \frac{2\eta P_{el}}{bl\rho c} \int_0^t dt' \int_{vt'-b}^{vt'} dx' \int_{-l/2}^{l/2} dy' \cdot$$
$$\int_{-\infty}^{\infty} dz' \delta(z') k(\vec{x} - \vec{x}', t - t'), \qquad (2)$$

with the power fraction η absorbed by the target ($1 - \eta$ is backscattered), the Dirac delta function δ, and the three-dimensional heat kernel[14]

$$k(\vec{x} - \vec{x}', t - t') = \frac{1}{(4\pi\alpha(t - t'))^{3/2}} \cdot$$
$$\exp\left(-\frac{(x - x')^2 + (y - y')^2 + (z - z')^2}{4\alpha(t - t')}\right). \qquad (3)$$

Spatial integration and evaluation at the position of the maximum temperature $x = vt, y = 0, z = 0$ results in

$$T(vt, 0, 0, t) = \frac{\eta P_{el}}{2bl\sqrt{\pi\lambda\rho c}} \int_0^t dt' \frac{1}{\sqrt{t - t'}} \, \text{erf}\left(\frac{l/2}{\sqrt{4\alpha(t - t')}}\right) \cdot$$
$$\left[\text{erf}\left(\frac{v(t - t')}{\sqrt{4\alpha(t - t')}}\right) - \text{erf}\left(\frac{v(t - t') - b}{\sqrt{4\alpha(t - t')}}\right)\right], \qquad (4)$$

where erf() is the error function. We provide a detailed derivation of Equation (4) in the Appendix. We performed the integration over time numerically with Python.

In the limit of short exposure times $t = b/v$, Oosterkamp[15,16] derived the maximum temperature increase by simplifying the heat conduction to a one-dimensional problem,

$$T_{cond} = \frac{2\eta P_{el}}{l\sqrt{\pi\lambda\rho cbv}}. \qquad (5)$$

Oosterkamp[15] defined the requirement for short exposures as

$$1.5 < \frac{b}{4\sqrt{\alpha t}} = \sqrt{\frac{b\rho cv}{16\lambda}}, \qquad (6)$$

when lateral heat conduction can be neglected. Assuming a surface velocity v of 200m/s, the focal spot width b needs to be larger than 11.5 μm to fulfill condition (6).

Heat capacity limit

In the limit of very short exposure times, the heat conduction is small compared to the electron transport that can here not be neglected, and only heat capacity determines the temperature increase at the focal spot. The expected maximum temperature increase in this heat capacity limit is given by

$$T_{cap} = \left\langle \frac{\delta P_{el}}{\delta V} \right\rangle_{max} \frac{b}{\rho cv}, \qquad (7)$$

where $\langle \frac{\delta P_{el}}{\delta V} \rangle_{max}$ is the maximum heat power density. The power P_{el} can be written as a product of the number of incoming electrons N_{el} and their primary energy E_{el}, $P_{el} = N_{el} E_{el}$. The introduction of the electron penetration depth

$$d = \frac{E_{el}}{\langle \frac{\partial E_{el}}{\partial z} \rangle_{max}}, \qquad (8)$$

as defined in Bartzsch and Oelfke,[11] with the maximum energy absorption per depth interval $\langle \frac{\partial E_{el}}{\partial z} \rangle_{max}$ allows to rewrite Equation (7) into

$$T_{cap} = \frac{P_{el}}{l\rho cvd}. \qquad (9)$$

At the transition between heat conduction and heat capacity limit, both mechanisms alone would lead to the same temperature rise. This transition is reached at a

focal spot width of

$$b_t = \frac{4\eta^2 \rho c v d^2}{\pi \lambda},$$ (10)

which was deduced assuming equal temperature changes in Equations (5) and (9).

2.1.2 | Simulations

We investigated the temperature increase locally at the focal spot by numerical simulations. The penetration of the electron beam into the focal track at the surface of the target was simulated using Monte Carlo simulations in TOPAS[17] (version 3.6.p1), which is based on Geant4. The applied G4EmPenelopePhysics list (fluorescence electrons, Auger electrons, and particle-induced x-ray emission activated; ignoring of deexcitation cuts deactivated) was particularly developed for Monte Carlo simulations of low-energy electromagnetic particle interactions.[18] The focal track was assumed to consist of pure tungsten, and the energy deposit was scored in voxels with a size of $1 \times 400 \times 1 \mu m^3$ ($x \times y \times z$). The parallel electrons (10^8 primaries) had an energy of 300 keV and were homogeneously distributed in a rectangle of 50 μm width (x-direction) and 30 mm length (y-direction), see Figure 1c. Additional to the homogeneous, rectangular electron distribution, we investigated an electron distribution based on the phase space resulting from previous simulations of the electron accelerator for the LFxT.[12] Here, the electron beam had full widths at half maximum of $50 \mu m \times 20 mm$. The energy deposit per voxel was converted into heat power density using Matlab (version 2018b, The MathWorks, Inc., Massachusetts, USA) and normalized to a primary electron current of 0.3 A.

The heat imparted leads to a temperature increase, which was simulated over a time frame of 5 μs with transient FEA using COMSOL Multiphysics (version 5.6, COMSOL AB, Stockholm, Sweden). The heat source passed along a focal track made of pure tungsten ($\rho = 19300 kg/m^3$, $c = 138 J/kg/K$, $\lambda = 170 W/m/K$) with a velocity of $v = 200 m/s$. The only considered heat dissipation mechanisms were electron transport and heat conduction. For the rectangular focal spot, the normalized heat power density was imported into a two-dimensional model in COMSOL Multiphysics as a cut through the center of the heat source ($y = 0$). The simulation volume was $1 \times 1 mm^2$ with a quadratic mapped mesh with an element size of 1 μm^2. For the focal spot based on the phase space of the electron beam, we used three dimensions for the heat power density and a target model of $0.5 \times 30 \times 0.5 mm^3$ with a hexahedral swept mesh with an element size of $(7 \mu m)^3$ (due to computational limits). Infinite element domains at all faces except the target surface, which had the Neumann boundary condition $\frac{\partial T}{\partial z} = 0$, mimicked a target layer.

Increasing the focal spot width beyond the transition width b_t increases the share of heat conduction and decreases the share of heat capacity in the total heat absorption. We investigated the transition between the heat capacity limit and the heat conduction limit by varying the focal spot width between 10 μm and 20 mm and adjusting the simulation time between 1 μs and 170 μs for a steady maximum temperature at the focal spot. To validate the applicability of the heat conduction limit and the heat capacity limit, we simulated surface heat sources that did not consider the electron penetration into the target and volumetric heat sources with no heat conduction in the target ($\lambda = 0$), respectively.

2.2 | Thermal benchmarking at the focal spot

The electron beam induces a considerable, strongly localized temperature increase at the focal spot. This temperature increase leads to thermal stress in the focal track due to high thermal gradients and different expansion coefficients of the focal track and target carrier materials. The focal track made of a tungsten–rhenium alloy and the target carrier made of titanium-zircon-molybdenum (TZM) are manufactured as one compound by powder forging. Unknown material parameters render a numeric assessment of the interface between the two materials very difficult. Moreover, FEA tools usually do not incorporate microscopic effects such as recrystallization or phase changes, making them unreliable to predict the material behavior at extreme temperature conditions.

In order to asses the strength of the tungsten–rhenium focal track, we benchmarked the focal spot parameters to a commercial x-ray tube that has similar thermal characteristics. The Straton x-ray tube (Siemens Healthineers AG)[19] is a high power, rotating envelope tube, which utilizes mainly convective cooling of the anode. For the Straton x-ray tube, we calculated the maximum temperature increase according to the heat conduction (5) and heat capacity limit (9) and compared them to the respective values of the LFxT.

The focal track of both the Straton x-ray tube and the LFxT consists of a tungsten–rhenium alloy (W-5%Re), for which we assumed $\rho = 19\,400 kg/m^3$, $c = 133 J/kg/K$, and $\lambda = 78 W/m/K$.[20,21] The Straton x-ray tube has a focal track radius of 48 mm and a rotation frequency of 150 Hz,[19] which lead to a surface velocity of $v = 45.2 m/s$. The maximum surface power density is obtained with the x-ray focal spot of $0.6 \times 0.7 mm^2$, where the Straton x-ray tube can withstand a total electron beam power of 42 kW for 20 s.[19] An anode angle between 7° and 9°[22] leads

to an exposed surface of $A = 2.68 - 3.45\,mm^2$ and a surface power density of $1.22 \cdot 10^{10}$–$1.56 \cdot 10^{10}W/m^2$. Additionally, we calculated the temperature increase for an electron beam power of 25 kW according to Monte Carlo simulations of 150 keV electrons considering backscattering (see Section 2.3). In the LFxT, the electron beam of $0.05 \times 20\,mm^2$ deposits a total power of 90 kW perpendicularly onto the target. The surface power density is therefore $9.0 \cdot 10^{10}$ W/m^2.

2.3 | Backscattering electrons

A large fraction of the electrons hitting the target are backscattered.[23] In the LFxT, the whole vacuum chamber is on the same electric potential as the target, and no electric field exists inside the vacuum chamber. Backscattered electrons travel in the field-free vacuum on straight paths and deposit their energy as heat onto the vacuum chamber walls.

We investigated the resulting temperature increase of the vacuum chamber with Monte Carlo simulations in TOPAS[17] (version 3.6.p1) and FEA in Ansys Mechanical (version 19 R3, Ansys, Inc., Pennsylvania, USA). The setup in both simulation tools was a simplified CAD model (Figure 1b), including the vacuum chamber walls, the target, the rotating shaft, the end of the electron beamline, the x-ray exit window, and further viewports. A hexahedral mesh was chosen in the FEA with an edge length of 1 mm.

In the Monte Carlo simulations, an electron beam (10^9 primaries) of 300 keV based on the phase space of the electron accelerator[12] hit the focal track, which was made of pure tungsten having substantially the same backscattering characteristics as a tungsten–rhenium alloy (W-5%Re). The produced photons were collected in a hemispherical phase space detector. The energy deposit of the backscattered electrons and produced photons was scored in all components of the vacuum chamber, which were modeled as iron. We transformed the scored energy into heat power density and normalized it to a primary electron beam current of 0.3 A using Python. With transient FEA, we simulated the temperature of the vacuum chamber made of stainless steel (AISI 316L) with the normalized heat power density as a heat source during the 20 s irradiation time. In a first assessment, there was no cooling included. For a more practicable simulation, we added active cooling pipes at the back wall of the vacuum chamber with a heat transfer coefficient of $\alpha = 35\,000$ W/m^2/K,[24] and an ambient temperature of 60 °C. Thermal radiation was neglected.

2.4 | Cooling concepts

Efficient active cooling of the target is crucial for high doses per exposure and short idle times. We investi-

gated four global cooling scenarios by transient FEA in Ansys Mechanical and simulated four irradiation cycles each of 20 s electron beam exposure followed by 20 min cool down as a conservative estimation for the temperature to re-equilibrate. The strongly simplified CAD model (as presented in Figure 1b with a different diameter and number of drive shafts) consisted of a cylindrical target with a diameter of 300 mm made of TZM ($c = 250$ J/kg/K, $\lambda = 142$ W/m/K, $\rho = 10\,300$ kg/m^3) and mounted on two drive shafts made of stainless steel (AISI 430) ($\rho = 7700$ kg/m^3, $c = 460$ J/kg/K, $\lambda = 25$ W/m/K). Rotation was neglected for the solely thermal concept analysis. A homogeneous heat source of 90 kW was applied to the focal track since a full resolution of the micrometer-sized focal spot would have caused computational issues. We conservatively ignored electron backscattering, and 100% of the thermal power was applied to the focal track.

Scenario 1 in Figure 2 illustrates the most simple case without any cooling so that the thermal energy was dissipated by radiation only with a radiation coefficient ϵ of 0.3,[25] and an ambient temperature of 40 °C. There was no contact between the drive shaft and the vacuum housing. This scenario represents a rotating anode with ball bearings. For scenario 2, liquid metal served as a lubrication fluid in a sliding bearing. A thermal contact thus enabled heat conduction from the rotating to the stationary parts of the drive shaft and thereby to the housing, in addition to the thermal radiation. Friction in the sliding bearing, which may become an additional heat source of up to 5 kW, was neglected. In scenario 3, an additional water cooling was installed through the main rotation axis of the drive shaft, resulting in a convective heat flow. We chose a heat transfer coefficient of $\alpha = 100\,00$ W/m^2/K[26] (the heat transfer coefficient depends on the coolant volume flow, which differs for different cooling sites) with a coolant temperature of 25°C. In scenario 4, cooling brackets were moved toward the target after each irradiation cycle. Realistically, one has to take into account the time to stop the target rotation before the brackets can come into contact. A direct contact of the brackets to the target material allowed heat conduction. Perfect heat transfer was assumed, while keeping the parameters from scenario 3.

2.5 | Target design

The design of the x-ray target is critical for the operation of the LFxT at high dose rates. A small focal spot size and high x-ray power require the operation well in the heat capacity limit and thus a target velocity in the order of 200 m/s. Only a sufficiently high heat capacity of the target and a long focal track allow coping with the extreme thermal power and applications of a few 100 Gy MRT peak dose in a single exposure.
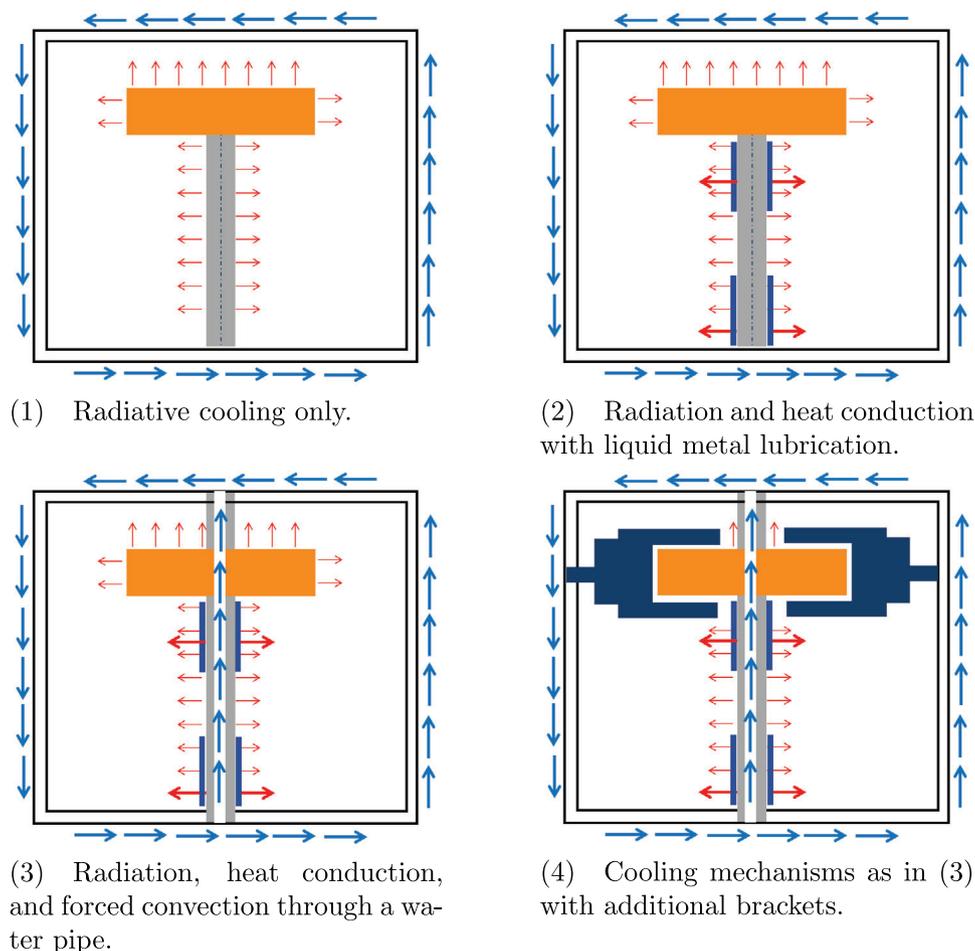
(1)   Radiative cooling only.

(2)   Radiation and heat conduction with liquid metal lubrication.

(3)   Radiation, heat conduction, and forced convection through a water pipe.

(4)   Cooling mechanisms as in (3) with additional brackets.

FIGURE 2   Four scenarios for the cooling study with thermal radiation (red arrows) and convection (blue arrows). The models consisted of a cylindrical target (orange), a drive shaft (gray), and a vacuum chamber housing (black double line)

Today, most high-performance x-ray targets are based on molybdenum and tungsten–rhenium alloys as a balance between high x-ray production efficiency, a high melting point, high thermal conductivity, and a high mechanical strength. In common powerful x-ray anodes, the outer diameter of the rotating anode is up to 200 mm with rotation speeds of 50–100 Hz.[23] However, due to the LFxT requirements on focal track length, surface velocity, and heat capacity, we chose a larger target with a diameter of around 240 mm at a rotation speed of 200 Hz. This upscaling results in greater rotation-induced mechanical stresses. In the design process, we aimed to reduce the mechanical stresses by choosing an adequate target profile, adding relief wells, and increasing the target thickness up to 50 mm to balance thermally induced bending due to a non-uniform thermal input. Another important aspect of the target design was the interface to rotor and motor drive, which has to withstand thermally induced and rotation-induced radial expansion. The axial strains are compensated with a nut spring mechanism, which will not be of further consideration within this article.

In another global transient FEA, we assessed the von Mises stresses and temperatures since metals lose mechanical strength at higher temperatures. To reduce computational load, we calculated on a 30° segment of the target with rotationally symmetric boundary conditions and applied 1/12 of the total beam power. The thermal load was homogeneously distributed onto the focal track due to large differences in time and space resolution between the local numerical assessment at the focal spot and the global analysis of the target. At the interface of the target and the drive shaft, we defined the heat transfer coefficient of $\alpha = 5000 \text{W/m}^2/\text{K}$ to the carrying rotor with respect to the heat transfer model developed by Mikić.[27] The driving design criterion was the 0.2% yield strength (0.2% yield strength represents the stress of a test specimen with a plastic deformation of 0.2%, we hence only considered linear-elastic material behavior). We simulated two scenarios. First, we rotated the target at full speed and had a total beam power of 90 kW for 20 s for a conservative estimate of the mechanical stresses. Second, we took the backscattering electrons into account and reduced the beam

power to a conservative estimate of 60 kW (compared to Section 3.1) with the target rotation decelerated linearly after 20 s with a breaking torque of 5.0 N m.

3 | RESULTS

3.1 | Focal spot: Heat conduction limit and heat capacity limit

The total electron beam power onto the target was 90 kW, whereof 55 kW, that is, 61% was absorbed by the target creating a volumetric heat source. The maximum heat power density in a depth of 5 μm was $2.0 \cdot 10^{15} \text{W/m}^3$ for the homogeneous, rectangular focal spot and $7.5 \cdot 10^{15} \text{W/m}^3$ for the phase space-based focal spot, respectively. For the heat capacity limit, the Monte Carlo simulations resulted in an electron penetration depth d of 29.7μm.

The transient FEA simulations transformed the heat power density that moved along the target volume into a temperature distribution. The temperature increased by a maximum of 157 K for the rectangular focal spot and by 483 K for the focal spot based on the phase space of the electron beam, respectively. The higher maximum temperature of the focal spot based on the phase space compared to the rectangular focal spot was caused by a shorter focal spot length and by the inhomogeneity of the electron distribution.

The simulations of different focal spot widths confirmed the transition between the heat conduction and heat capacity limit in dependence on the spot width. The FEA simulations ignoring electron penetration reproduced the theoretically expected temperature increase at the focal spot in the heat conduction limit (see Figure 3). The FEA simulations of volumetric heat sources with disabled heat conduction confirmed the heat capacity limit. Here, the temperature increase at the focal spot was independent of the focal spot width, as predicted by Equation (9).

The full simulations including electron penetration and heat conduction resulted in a maximum temperature increase that was lower than predicted by either limit (see Figure 3) because both energy dissipation mechanisms contributed. The full simulation at the transition focal spot width b_t of 1.3 mm resulted in a temperature rise of 109 K, whereas both limits predicted 190 K. The broader the focal spot width, the more the temperature increase converged to the prediction by the heat conduction limit. At 20 mm focal spot width, the simulated temperature increase was less than 20% below the prediction by the heat conduction limit. At focal spot widths much smaller than b_t, the maximum temperature increase converged to the prediction by the heat capacity limit. As the focal spot width decreased, the temperature increase predicted by the heat capacity limit

became much smaller as compared to the heat conduction limit.

The LFxT operates far in the heat capacity limit with a surface velocity of 200 m/s, a focal spot width of 50 μm, and an acceleration voltage of 300 kV. In contrast, the Straton x-ray tube operates in the heat conduction limit: With an electron energy of 150 keV, a penetration depth d of 10.8 μm resulting from Monte Carlo simulations, and a surface velocity of 45 m/s, the focal spot width of 0.6 mm is an order of magnitude larger than the transition focal spot width of 0.04 mm.

3.2 | Thermal benchmarking at the focal spot

We compared the expected temperature increase at the focal spot of the LFxT with the respective value of the Straton x-ray tube. As described in Section 3.1, the LFxT operates in the heat capacity limit as its focal spot is much narrower than the transition focal spot width, whereas the Straton x-ray tube operates in the heat conduction limit as its focal spot is much broader than the transition width. While for the LFxT, the temperature increased by $T_{\text{LFxT}} = 294\text{K}$, the temperature increase at the focal spot of the Straton x-ray tube was $T_{\text{Strat}} = 4531\text{K}$ (or $T_{\text{Strat,cap}} = 7446\text{K}$ according to the heat capacity limit). As thermal stress is related to the temperature gradient at the focal spot, we expect considerably lower stresses for the LFxT compared to the commercial Straton x-ray tube with similar power characteristics.

The temperature increase for the LFxT was higher than the respective value obtained in Section 3.1. The reason was a conservative estimate with the total primary electron power as input power and the shorter focal spot length. The temperature increase for the Straton x-ray tube was higher than the recommended maximum temperatures for a typical tungsten–rhenium alloy.[20,25] However, considering backscattered electrons reduced the absorbed power from 42 kW to 25 kW, which reduced the expected temperature increase of $T_{\text{Strat,25kW}} = 2734\text{K}$ to an acceptable range.

3.3 | Backscattering electrons

The proportion of backscattered electrons was 49% of the number of primary electrons, which corresponded to 34 kW, that is, 38% of the primary electron energy. The energy of the produced x-rays made up for only $(0.56 \pm 0.01)\%$ (standard deviation) of the primary electron energy. Monte Carlo simulations provided the heat power density distribution in the vacuum chamber and the other x-ray tube components caused by backscattered electrons and produced photons. At the end of
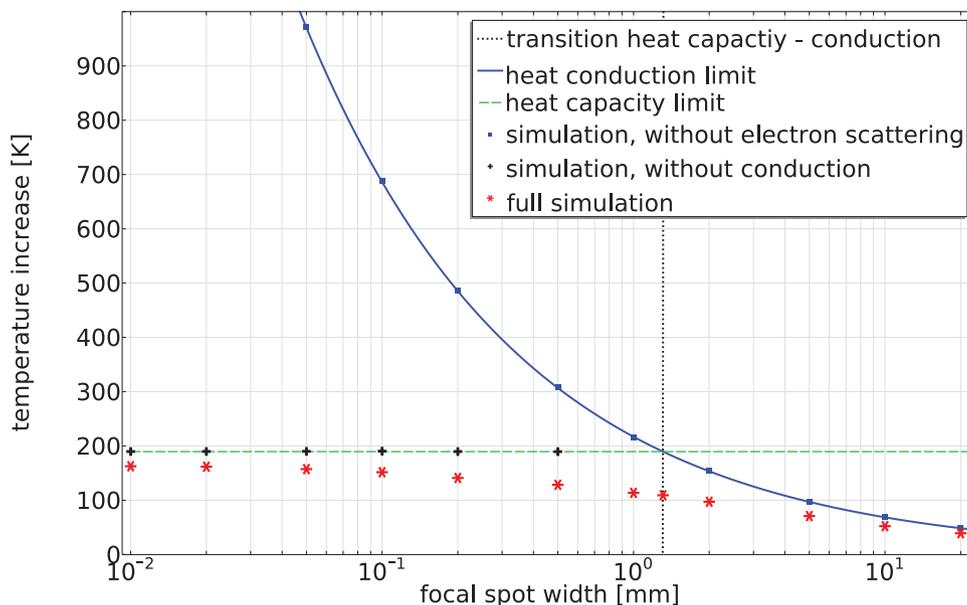
FIGURE 3 Maximum temperature increase at the focal spot in the heat capacity limit (small spot widths) and the heat conduction limit (broad spot widths) as calculated in Monte Carlo simulations and transient FEA. The electron beam had a power of 90 kW and an energy of 300 keV, the target surface velocity was 200 m/s
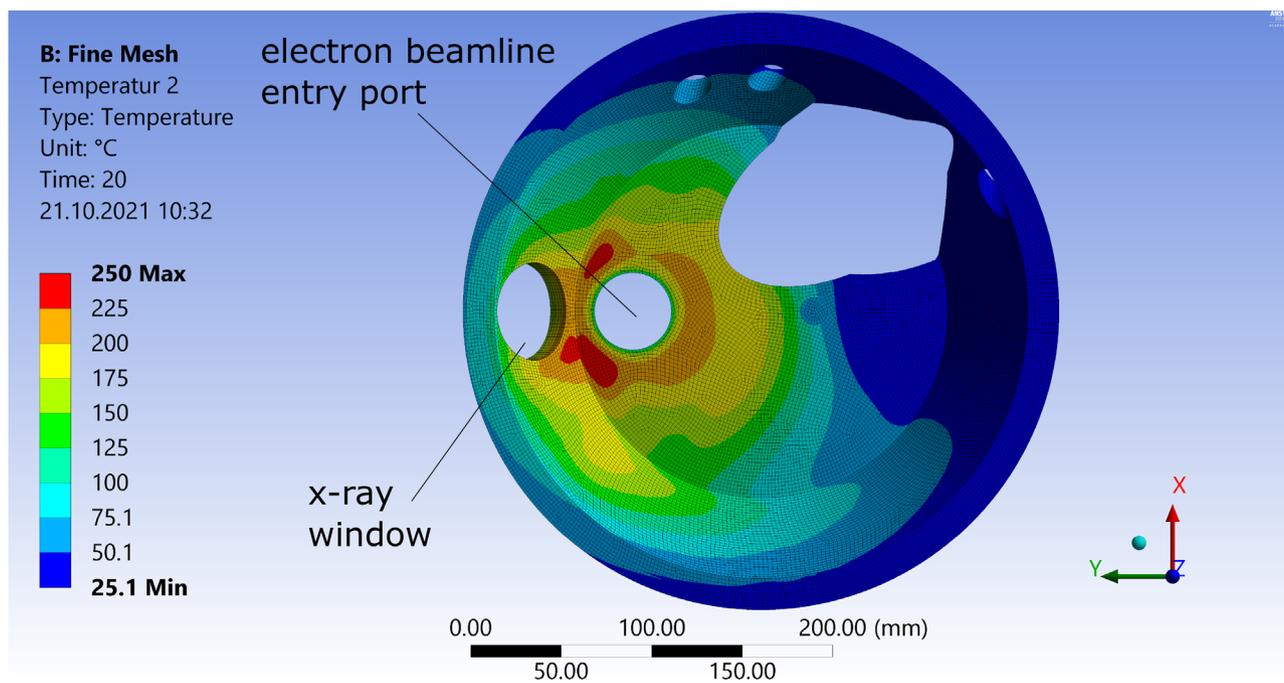

FIGURE 4 Temperature distribution at the inner surface of the vacuum chamber after 20 s irradiation time with active cooling

a 20 s exposure at 90 kW electron beam power, the highest temperatures of almost 700 °C were reached at the x-ray window and at the electron beamline entry port. With active cooling through cooling channels of the back wall, the maximum temperature reached 250 °C at the same positions as without cooling, see in Figure 4.

3.4 | Cooling concepts

Figure 5 shows the course of the maximum temperature in the TZM target during four cycles of electron beam exposure. With radiative cooling only (scenario 1), the temperature increased from cycle to cycle and reached a maximum of almost 1300 °C in the fourth cycle, see
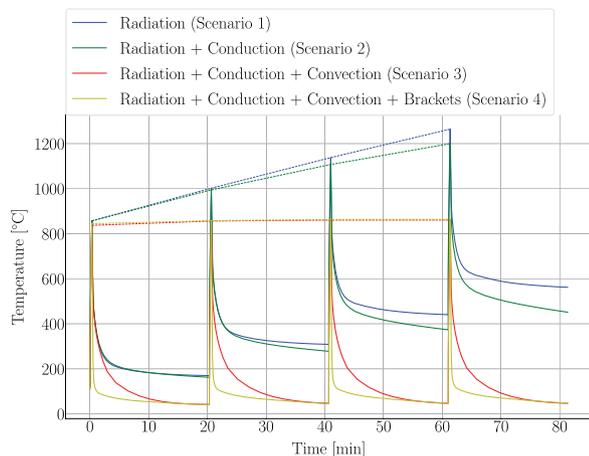
FIGURE 5 Maximum focal track temperatures of four global cooling concepts during four cycles of beam exposure and cooling

Figure 5. After 20 min cooling, the maximum temperature dropped to approximately 580 °C in the fourth cycle. In scenario 2, the housing acted as an additional heat sink, causing however only a slight drop of the maximum temperature, which was approximately 1200 °C after four cycles. The maximum temperature dropped to approximately 450 °C after cooling in the fourth cycle. Scenario 3 with convective water cooling showed a substantial drop in maximum temperature, which was almost constant at approximately 860 °C in all cycles at the end of the irradiation. The maximum temperature after cooling remained below 46 °C and did not show a considerable increase from cycle to cycle. Scenario 4 yielded a much faster temperature drop in the beginning of the cooling period than scenario 3. After applying the brackets, the temperature decreased below 100 °C in less than 2 min. The temperature at the end of the cooling period matched the value of scenario 3.

3.5 | Target design

Figure 6 illustrates the profile of the LFxT target, designed with the aim to maximize the target diameter and thickness, to minimize mechanical stress, and to compensate for thermally induced bending. The tapered part is designed for equal strength by decreasing the thickness with distance from the rotation axis. The maximized inner radius, R_{base}, enables the highest possible heat exchanging surface. The heating induced by the electron beam only occurs on the upper side resulting in an asymmetrical thermal expansion. The width of the target, t_{tip}, is larger compared to conventional anodes in order to counteract the asymmetrical thermal expansion maintaining a plane surface for constant focal spot dimensions. Relief wells and a segmented surface (not shown) reduce the mechanical stress.

Braking of the target directly after irradiation can substantially reduce mechanical stresses. Since material strength decreases at higher temperatures, we show the stress–temperature curves at the inner radius of the target (R_{base}) in Figure 7. The maximum strength depicted refers to a stress-relieved sheet metal of 2 mm thickness made of TZM. The minimum strength refers to the recrystallized state of the sheet metal. Depending on the degree of deformation during the manufacturing process, the expected strength is approximately the average between the minimum and maximum[28] (project meeting with an x-ray anode manufacturer, March 2021).

4 | DISCUSSION

We investigated the heat management of an LFxT prototype that we are currently setting up in our laboratory. The low electron-to-photon conversion efficiency of less than 1% renders efficient methods of heat dissipation essential for the development of an x-ray tube delivering UHDRs. In simulations, we showed the transition from the heat conduction to the heat capacity limit, we investigated the thermal load to components close to the focal spot, and assessed thermomechanical stress of the x-ray target. Our simulations demonstrate the feasibility of the LFxT prototype with active cooling.

The transient FEA of a volumetric heat source confirmed both the heat conduction limit for focal spot widths much broader than the transition width and the heat capacity limit for widths much narrower than the transition width. Focal spot widths around the transition resulted in a substantially lower temperature increase than predicted by either limit, which demonstrated that the heat diffusion length and the electron penetration depth were similar, as presumed by Bartzsch and Oelfke.[11]

Monte Carlo simulations provided the heat power P for the heat conduction limit and the electron penetration depth d for the heat capacity limit. We found that the electron penetration depth d depended on the used physics list and on the version of TOPAS or Geant4. Simulations with older versions of Geant4 resulted in substantial differences in d (shorter by > 10%), which can possibly be attributed to changes in the low-energy data set G4EMLOW related to elastic scattering of photons or to rare energy nonconservation in the G4PenelopeComptonModel.

The beneficial lower temperature increase in the heat capacity limit compared to the heat conduction limit for focal spot widths smaller than the transition width was clearly demonstrated. We could thus show that the LFxT operates in the heat capacity limit, where the temperature increase was far lower than in the heat conduction limit. With the heat capacity limit, the LFxT has a great potential not only for MRT and FLASH radiotherapy but also for phase contrast imaging where very small focal spot sizes are necessary.[29]

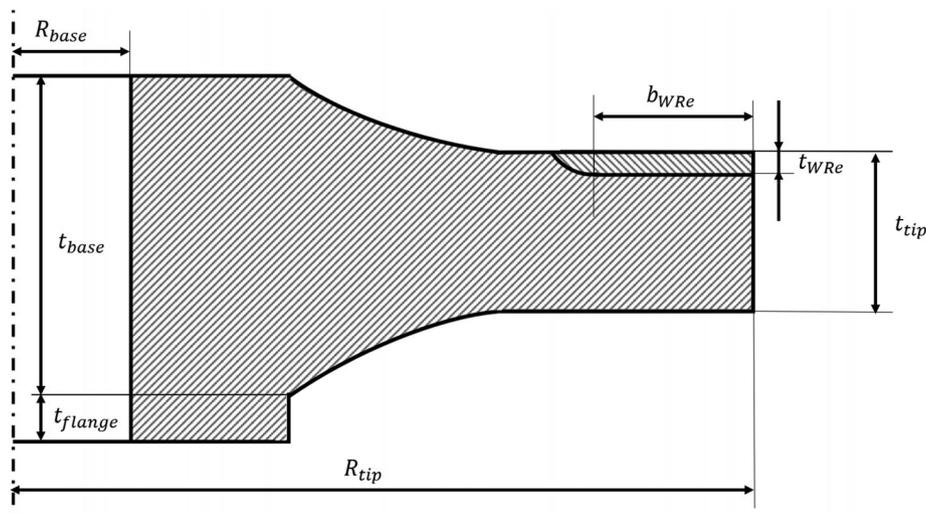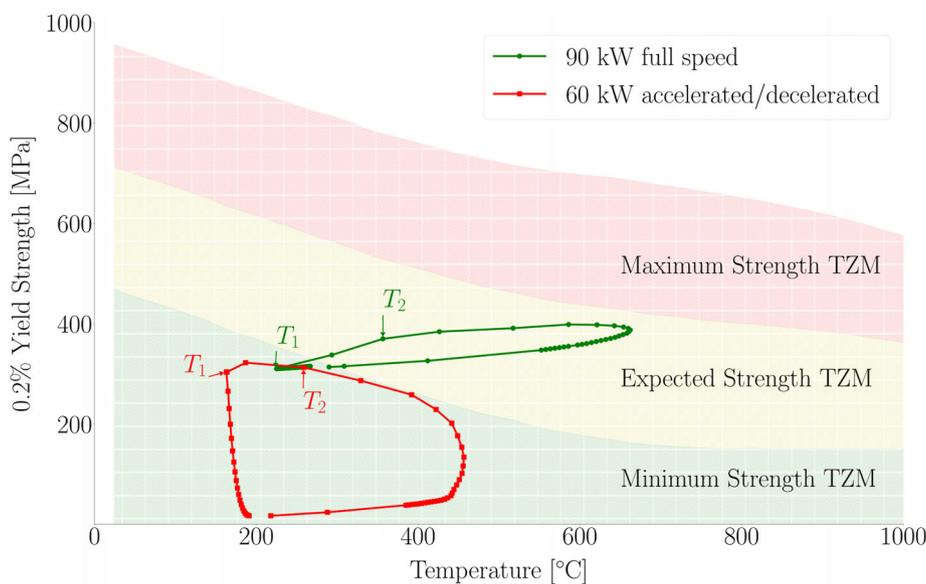For the assessment of thermal stresses at the focal spot, the benchmark method was not the most

FIGURE 6 Target geometry. R denotes the radius, t the thickness, and WRe the tungsten–rhenium alloy of the focal track

Time	Temperature	Stress
$T_{1,90\,kW}$	223.7 °C	310.1 MPa
$T_{2,90\,kW}$	356.6 °C	383.6 MPa
$T_{1,60\,kW}$	162.2 °C	303.4 MPa
$T_{2,60\,kW}$	258.6 °C	312.6 MPa

FIGURE 7 Stress temperature relationship at the inner target diameter during the fourth irradiation cycle. T_1 indicates the start of irradiation and T_2 the end of irradiation. The green line represents the total beam power and a continuous rotation of the target wheel. The red line considers backscattered electrons and braking of the target after irradiation

specific approach to analyze the complex material pairing and deformation effects between the tungsten track and the TZM carrier material. The estimated temperature increase at the focal spot of the Straton x-ray tube might be slightly higher than during operation because we only considered a tungsten–rhenium alloy as focal track material instead of including further material layers with a higher thermal conductivity. However, the commercially available Straton x-ray tube tolerates thermal conditions that are more extreme than expected for the LFxT operating in the heat capacity limit, even when considering the total electron beam power of the LFxT as

a conservative assumption. For this reason, the LFxT should operate safely given the viability of the benchmark source.

In the manufacturing process of the target, the tungsten–rhenium layer is pressed and forged onto the TZM structure. Diameters larger than 240 mm and thicknesses bigger than 50 mm are beyond state-of-the-art manufacturing limits. As we showed in Figure 7, the conservative assumption of the total electron beam power of 90 kW transferred to the target reached the maximum of the expected strength, hence not leaving space for a safety margin. In contrast, consideration of backscattering electrons (60 kW transferred to the target) in combination with the 0.2% yield strength (rather than brittle failure) created a safety margin in the design. For more precise results, it would be interesting to further develop the FEA material models to deal with nonlinear plastic deformations and phenomena like brittle to ductile transition. It is challenging to perform design life calculations since the results are highly dependent on the manufacturing technique, the target carrier material quality, the test specimen dimensions, and the degree of deformation as stated by Calderon et al.[30] However, no significant losses in strength due to fatigue have been reported until 10^4 electron beam exposures. In future anode designs, it might be of interest to consider carbon fiber reinforced carbon as a potential carrier material because of a higher specific strength (in terms of the ratio between strength and density) and a smaller thermal expansion coefficient.

The vacuum chamber wall opposite the focal spot needs active cooling, especially around the beamline and the x-ray window, to keep the temperature of all vacuum chamber components within their allowed range below 400 ° C, which depends on the desired vacuum quality of at least 10^{-6} millibar . Neither the x-ray window nor the electron beamline nor the vacuum chamber itself can withstand the high temperatures that are expected without active cooling. Moreover, desorption and hydrogen diffusion through the vacuum chamber wall occur more readily for higher temperatures of the stainless-steel chamber. For this reason, the temperature of the vacuum chamber should be kept as low as possible. Further critical components are the quadrupole magnets, located outside the vacuum chamber close to the transition between the beamline and the vacuum chamber. Even though the magnets are thermally insulated from the vacuum chamber, thermal radiation from the beamline heats the magnets. Since the heat power densities at the target and at the opposing vacuum chamber wall are comparable, there is no effective radiation cooling during the beam exposure. The radiation cooling provides a recognizable impact only after the vacuum chamber wall has been cooled down.

Cooling scenarios 1 and 2 are neglected for further consideration, since radiative cooling and a sliding bearing contact only would lead to a failure of the target due to too high temperatures. The greatest cooling efficiency was exhibited in scenario 4 with a thermal contact between rotating and stationary parts, an active pipe cooling, and cooling brackets. This was expected because of the additional heat sinks. The fast temperature drop can be valuable for high repetition rates for a clinical application of the LFxT. However, there is a risk of applying cooling brackets as the steep temperature drop could cause embrittlement of the focal track. The rapid cooling could further drive hardening and inner stresses due to different thermal expansion coefficients of tungsten–rhenium and TZM. For these reasons, we consider scenario 3 as a suitable solution for the further LFxT development since it showed a similar temperature evolution to scenario 4 without the extra expense and risk of installing cooling brackets. Nevertheless, the simulated cooling over 20 min was not sufficient to lower the anode temperature to room temperature in any scenario. The main reason for this inefficacy was the distance that the heat had to diffuse from the focal track via the intersection between target wheel and drive train to the inner convective cooling pipe, which had a small cross section and thus a small heat exchanging surface.

5 | CONCLUSIONS

At the focal spot, we have validated the heat capacity limit for the LFxT with numerical simulations, which allows much higher electron beam power densities than the heat conduction limit found in conventional x-ray tubes. Active cooling through the target shaft and at the vacuum chamber housing will facilitate a stable operation of the LFxT prototype that we are currently constructing for preclinical MRT research and as a proof of the LFxT concept. With a higher electron beam power, the LFxT seems promising for the clinical application of MRT and FLASH treatments. When upgrading the system to higher powers, the induced thermomechanical stress at the target is the limiting factor. The use of alternative target materials, such as carbon fiber reinforced carbon, will likely be necessary to achieve operation at 1.5 MW.

CONFLICT OF INTEREST
The authors have no conflicts to disclose.

ORCID
Johanna Winter
https://orcid.org/0000-0002-3825-399X

Christian Petrich (ORCID)
https://orcid.org/0000-0002-5002-4719
Stephanie E. Combs (ORCID)
https://orcid.org/0000-0002-6934-2864
Marek Galek (ORCID)
https://orcid.org/0000-0002-6983-9758
Ghaleb Natour (ORCID)
https://orcid.org/0000-0002-8068-8989
Michael Butzek (ORCID)
https://orcid.org/0000-0001-9634-3611
Jan J. Wilkens (ORCID)
https://orcid.org/0000-0002-1851-0581
Stefan Bartzsch (ORCID)
https://orcid.org/0000-0001-9550-9122

REFERENCES

1. Delaney GP, Barton MB. Evidence-based estimates of the demand for radiotherapy. *Clin Oncol*. 2015;27:70-76.
2. Slatkin DN, Spanne PO, Dilmanian FA, Sandbora M. Microbeam radiation therapy. *Med Phys*. 1992;19:1395-1400.
3. Laissue JA, Blattmann H, Di Michiel M, et al. Weanling piglet cerebellum: a surrogate for tolerance to MRT (microbeam radiation therapy) in pediatric neuro-oncology. In: *Proceedings of SPIE*, Barber HB, Roehrig H, Doty FP, Schirato RC, Morton EJ (eds.) volume 4508, International Society for Optics and Photonics, 2001:65-73.
4. Bartzsch SH, Corde S, Crosbie JC, et al. Technical advances in X-ray microbeam radiation therapy. *Phys Med Biol*. 2020;65:02TR01.
5. Favaudon V, Caplier L, Monceau V, et al. Ultrahigh dose-rate FLASH irradiation increases the differential response between normal and tumor tissue in mice. *Sci Transl Med*. 2014;6:245ra93.
6. Mazal A, Prezado Y, Ares C, et al. FLASH and minibeams in radiation therapy: the effect of microstructures on time and space and their potential application to protontherapy. *Br J Radiol*. 2020;93:20190807.
7. Wilson JD, Hammond EM, Higgins GS, Petersson K. Ultra-high dose rate (FLASH) radiotherapy: silver bullet or fool's gold?. *Front Oncol*. 2020;9:1563.
8. Duncan M, Donzelli M, Pellicioli P, et al. First experimental measurement of the effect of cardio-synchronous brain motion on the dose distribution during microbeam radiation therapy. *Med Phys*. 2020;47:213-222.
9. Montay-Gruel P, Bouchet A, Jaccard M, et al. X-rays can trigger the FLASH effect: ultra-high dose-rate synchrotron light source prevents normal brain injury after whole brain irradiation in mice. *Radiother Oncol*. 2018;129:582-588.
10. Bourhis J, Sozzi WJ, Jorge PG, et al. Treatment of a first patient with FLASH-radiotherapy. *Radiother Oncol*. 2019;139:18-22.
11. Bartzsch S, Oelfke U. Line focus x-ray tubes-a new concept to produce high brilliance x-rays. *Phys Med Biol*. 2017;62:8600-8615.
12. Winter J, Galek M, Matejcek C, et al. Clinical microbeam radiation therapy with a compact source: specifications of the line-focus X-ray tube. *Phys Imaging Radiat Oncol*. 2020;14:74-81.
13. Oppelt A. *Imaging Systems for Medical Diagnostics: Fundamentals, Technical Solutions and Applications for Systems Applying Ionization Radiation, Nuclear Magnetic Resonance and Ultrasound*. 2nd ed. Publicis; 2005.
14. Evans LC. *Partial Differential Equations. Graduate Studies in Mathematics*. Vol 19. 2nd, revised ed. American Mathematical Society; 2010.
15. Oosterkamp WJ. The heat dissipation in the anode of an x-ray tube - I. Loads of short duration applied to stationary anodes. *Philips Res Rep*. 1948;3:49-59.
16. Oosterkamp WJ. The heat dissipation in the anode of an x-ray tube—II. Loads of short duration applied to rotating anodes. *Philips Res Rep*. 1948;3:303-317.
17. Perl J, Shin J, Schümann J, Faddegon B, Paganetti H. TOPAS: an innovative proton Monte Carlo platform for research and clinical applications. *Med Phys*. 2012;39:6818-6837.
18. Geant4 Collaboration. Penelope Models—Physics Reference Manual 10.7 documentation. Accessed November 10, 2021. https://geant4-userdoc.web.cern.ch/UsersGuides/PhysicsReferenceManual/html/electromagnetic/introduction/penelope.html.
19. Schardt P, Deuringer J, Freudenberger J, et al. New x-ray tube performance in computed tomography by introducing the rotating envelope tube technology. *Med Phys*. 2004;31:2699-2706.
20. Cardarelli F. *Materials Handbook—A Concise Desktop Reference*. 2nd ed. Springer; 2008.
21. Tanabe T, Eamchotchawalit C, Busabok C, Taweethavorn S, Fujitsuka M, Shikama T. Temperature dependence of thermal conductivity in W and W-Re alloys from 300 to 1000 K. *Mater Lett*. 2003;57:2950-2953.
22. Flohr T, Ohnesorge B. Multi-slice CT technology. In *Multi-Slice and Dual-Source CT in Cardiac Imaging*, Ohnesorge B, Flohr T, Becker CR, Knez A, Reiser MF eds. Springer; 2007:41-69.
23. Behling R. *Modern Diagnostic X-Ray Sources: Technology, Manufacturing, Reliability*. CRC Press; 2016.
24. Bohl W, Elmendorf W. *Technische Strömungslehre: Stoffeigenschaften von Flüssigkeiten und Gasen, Hydrostatik, Aerostatik, inkompressible Strömungen, kompressible Strömungen, Strömungsmesstechnik*. 13th, revised and expanded edn. Vogel-Fachbuch Kamprath-Reihe, Vogel, Würzburg, 2005.
25. Plansee SE. Wolfram Plansee. Accessed November 10, 2021. https://www.plansee.com/de/werkstoffe/wolfram.html.
26. VDI e.V. *VDI-Wärmeatlas*. 11th, revised and expanded ed. Springer Vieweg; 2013.
27. Mikić BB. Thermal contact conductance; theoretical considerations. *Int J Heat Mass Transfer*. 1974;17:205-214.
28. Plansee SE. Molybdän|Plansee. Accessed November 14, 2021. https://www.plansee.com/de/werkstoffe/molybdaen.html.
29. Momose A. Phase-sensitive imaging and phase tomography using X-ray interferometers. *Opt Express*. 2003;11:2303-2314.
30. Calderon HA, Kostorz G, Ullrich G. Microstructure and plasticity of two molybdenum-base alloys (TZM). *Mater Sci Eng, A*. 1993;160:189-199.
31. Griffiths DJ. *Introduction to Electrodynamics*. 4th ed. Pearson Education, Inc, 2013.

APPENDIX A: Derivation of the heat conduction limit

The derivation of the temperature increase *T* in the heat conduction limit starts with the heat equation,

$$\frac{\partial T}{\partial t} - \alpha \Delta T = f(\vec{x}, t), \tag{11}$$

with $\frac{\partial}{\partial t}$ the partial derivative with respect to time; $\alpha = \frac{\lambda}{\rho c}$ the thermal diffusivity with λ the thermal conductivity,

ρ the mass density, and c the specific heat capacity; Δ the Laplacian operator; and $f(\vec{x}, t)$ an external heat source in dependence of position $\vec{x} = (x, y, z)$ and time t. In the heat conduction limit, $f(\vec{x}, t)$ represents the electron beam of power P_{el}, width b, and length l passing over the surface of a half space ($z < 0$) with velocity v, η represents the power fraction absorbed by the target ($1 - \eta$ is backscattered or transformed into x-radiation),

$$f(\vec{x}, t) = \frac{\eta P_{el}}{bl\rho c} \cdot \Theta(x, b) \cdot \Theta(y, l) \cdot \delta(z)$$

$$= \frac{\eta P_{el}}{bl\rho c} \cdot \Theta(x - (vt - b)) \, \Theta(vt - x) \cdot$$

$$\Theta(y + l/2) \cdot \Theta(l/2 - y) \cdot \delta(z), \quad (12)$$

with the Heaviside step function Θ and the Dirac delta function δ.

By means of the method of image charges[31] (resulting in a factor 2), the solution of the three-dimensional heat equation can be obtained by

$$T(x, y, z, t) = \frac{2\eta P_{el}}{bl\rho c} \int_0^t dt' \int_{-\infty}^{\infty} dx' \int_{-\infty}^{\infty} dy' \int_{-\infty}^{\infty} dz' \cdot$$

$$\Theta(x' - (vt' - b)) \, \Theta(vt' - x') \, \Theta(y' + l/2) \cdot$$

$$\Theta(l/2 - y') \, \delta(z') \cdot k(\vec{x} - \vec{x}', t - t'), \quad (13)$$

with the three-dimensional heat kernel[14]

$$k(\vec{x} - \vec{x}', t - t') = \frac{1}{(4\pi\alpha(t - t'))^{3/2}} \cdot$$

$$\exp\left(-\frac{(x - x')^2 + (y - y')^2 + (z - z')^2}{4\alpha(t - t')}\right). \quad (14)$$

It follows

$$T(x, y, z, t) = \frac{2\eta P_{el}}{bl\rho c} \int_0^t dt' \int_{vt'-b}^{vt'} dx' \int_{-l/2}^{l/2} dy' \int_{-\infty}^{\infty}$$

$$\times dz' \delta(z') \cdot \frac{1}{(4\pi\alpha(t - t'))^{3/2}} \cdot$$

$$\times \exp\left(-\frac{(x - x')^2 + (y - y')^2 + (z - z')^2}{4\alpha(t - t')}\right)$$

$$= \frac{2\eta P_{el}}{bl\rho c} \frac{1}{(4\pi\alpha)^{3/2}} \int_0^t dt' \int_{vt'-b}^{vt'} dx' \int_{-l/2}^{l/2} dy' \cdot$$

$$\times \frac{1}{(t - t')^{3/2}} \exp\left(-\frac{(x - x')^2 + (y - y')^2 + z^2}{4\alpha(t - t')}\right).$$

$$\quad (15)$$

Spatial integration over y' results in

$$\int_{-l/2}^{l/2} dy' \exp\left(-\frac{(y - y')^2}{4\alpha(t - t')}\right) =$$

$$2\sqrt{\pi\alpha(t - t')} \, \mathrm{erf}\left(\frac{l/2}{\sqrt{4\alpha(t - t')}}\right), \quad (16)$$

where erf() is the error function.

The highest temperature is expected at the center of the focal spot ($y = 0$, $x = vt$) at the target surface ($z = 0$). With the above definition of the focal spot between $x_1 = vt - b$ and $x_2 = vt$, the point of interest $x = vt$ is directly at the end of the focal spot, that is, after the passing of the complete focal spot width, where the temperature is highest. Evaluation at $\vec{x} = (vt, 0, 0)$ and inserting Equation (16) into (15) yields

$$T(vt, 0, 0, t) = \frac{2\eta P_{el}}{bl\rho c} \frac{1}{4\pi\alpha} \int_0^t dt' \int_{vt'-b}^{vt'} dx' \cdot$$

$$\frac{1}{t - t'} \cdot \mathrm{erf}\left(\frac{l/2}{\sqrt{4\alpha(t - t')}}\right) \cdot \exp\left(-\frac{(vt - x')^2}{4\alpha(t - t')}\right). \quad (17)$$

Spatial integration over x' results in

$$\int_{vt'-b}^{vt'} dx' \exp\left(-\frac{(vt - x')^2}{4\alpha(t - t')}\right) =$$

$$\sqrt{\pi\alpha(t - t')}\left[\mathrm{erf}\left(\frac{v(t - t')}{\sqrt{4\alpha(t - t')}}\right) - \mathrm{erf}\left(\frac{v(t - t') - b}{\sqrt{4\alpha(t - t')}}\right)\right].$$

$$\quad (18)$$

Inserting Equation (18) into (17) yields

$$T(vt, 0, 0, t) = \frac{\eta P_{el}}{2bl\rho c\sqrt{\pi\alpha}} \int_0^t dt' \frac{1}{\sqrt{t - t'}} \mathrm{erf}\left(\frac{l/2}{\sqrt{4\alpha(t - t')}}\right) \cdot$$

$$\left[\mathrm{erf}\left(\frac{v(t - t')}{\sqrt{4\alpha(t - t')}}\right) - \mathrm{erf}\left(\frac{v(t - t') - b}{\sqrt{4\alpha(t - t')}}\right)\right]$$

$$= \frac{\eta P_{el}}{2bl\sqrt{\pi\alpha}\rho c} \int_0^t dt' \frac{1}{\sqrt{t - t'}} \mathrm{erf}\left(\frac{l/2}{\sqrt{4\alpha(t - t')}}\right) \cdot$$

$$\left[\mathrm{erf}\left(\frac{v(t - t')}{\sqrt{4\alpha(t - t')}}\right) - \mathrm{erf}\left(\frac{v(t - t') - b}{\sqrt{4\alpha(t - t')}}\right)\right], \quad (19)$$

which is identical to Equation (4).